2011 IEEE/RSJ International Conference on
Intelligent Robots and Systems
September 25-30, 2011. San Francisco, CA, USA

Deflection-Based Force Sensing for Continuum Robots: A Probabilistic Approach

D. Caleb Rucker, *Member, IEEE* and Robert J. Webster III, *Member, IEEE*

***Abstract*— The inherent flexibility of continuum robots allows them to interact with objects in a safe and compliant way. This flexibility also makes it possible to use robot deflection to estimate external forces applied to the robot. This "intrinsic force sensing" concept is particularly useful for thin continuum robots where application constraints preclude the use of traditional force sensors. This paper describes an Extended Kalman Filter approach to estimate forces applied at the tip of a continuum robot using only uncertain pose measurements and a kinematic-static model of the robot with uncertainty.**

I. INTRODUCTION

Many robot designs and architectures are inherently flexible. This is especially true for the broad class of "continuum" robots which are inspired by flexible biological entities such as tentacles, trunks, tails, snakes, and worms (see [1], [2], [3] for reviews). Because the basic structures of these robots are continuously flexible, their overall shapes and end-effector poses typically change significantly when external loads are applied. For many designs, this inherent compliance is often cited as a potential advantage for working safely within constrained environments, where inadvertent robot-environment contact is possible.

Recent research has shown that continuum robots can also be used as force senors. In [4], [5], Xu and Simaan introduced the concept of intrinsic force sensing for continuum robots, demonstrating that by sensing the actuation loads on their multi-backbone continuum robot, certain components of an applied end-effector wrench could be determined. Additionally, work by Bajo and Simaan used the relative position of points on the robot shape to determine the contact location [6]. The concept of using the robot itself as a force sensor appears promising for applications like minimally invasive surgery, where it is sometimes impractical to outfit the manipulator with commercial force sensors due to size constraints.

In this paper, we address intrinsic force sensing from a probabilistic perspective: given uncertain measurements of the robot's shape and/or end effector pose, we obtain a probability distribution for the external loads on the robot. Our approach is based on the applying the popular Extended Kalman Filter (EKF) algorithm to the problem of estimating the applied forces and the pose of the end-effector simultaneously.

A. Problem Statement

In the following investigation, we assume that a robot model exists of the form

$$\boldsymbol{p} = \boldsymbol{g}(\boldsymbol{\tau}, \boldsymbol{F}), \tag{1}$$

where $\boldsymbol{\tau}$ is a vector of actuator values, $\boldsymbol{F}$ is an externally applied force at the end effector, and $\boldsymbol{p}$ is the robot's end effector pose.

Then, our problem statement can be formulated as follows: The state of the robot is defined by the vector $\boldsymbol{x} = [\boldsymbol{p}^T \;\; \boldsymbol{\tau}^T \;\; \boldsymbol{F}^T]^T$. Given sensor measurements for $\boldsymbol{p}$ and $\boldsymbol{\tau}$, an initial estimate for $\boldsymbol{F}$, and the uncertainties in all these quantities, use the robot model and the Extended Kalman Filter to find the probability distribution for $\boldsymbol{x}$ which best represents the actual pose, actuator values, and applied force.

II. EXAMPLE ROBOT MODEL

The force sensing methodology developed in this paper is applicable to any flexible robot with a model of the form in (1). In order to demonstrate proof-of-concept for probabilistic force sensing, we will test our algorithms in simulation using a specific model for a tendon-actuated robot under external loading, which we derive in this section.

Cosserat rod theory has recently been used to describe the large nonlinear deflections of various continuum robot designs (see e.g. [7], [8], [9], [10]). Following Antman's thorough work on nonlinear elasticity

Manuscript received March 14, 2011, revised July 15, 2011. This material is based upon work supported in part by National Science Foundation grants CBET-0651803 and IIS-1054331,and in part by National Institutes of Health grant R44 CA134169.

D. C. Rucker and R. J. Webster III are with Vanderbilt University, Nashville, TN 37235, USA (e-mail: {daniel.c.rucker, robert.webster}@vanderbilt.edu).

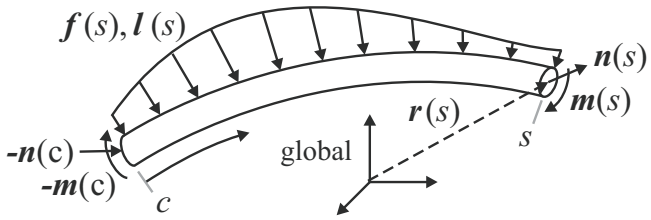

Fig. 1. Arbitrary section of rod from subject to distributed forces and moments. The internal forces $\boldsymbol{n}$ and moments $\boldsymbol{m}$ are also shown.

[11], we give the following equilibrium differential equations for a Cosserat rod:

$$\dot{\boldsymbol{n}}(s) + \boldsymbol{f}(s) = \boldsymbol{0}, \tag{2}$$

$$\dot{\boldsymbol{m}}(s) + \dot{\boldsymbol{r}}(s) \times \boldsymbol{n}(s) + \boldsymbol{l}(s) = \boldsymbol{0}. \tag{3}$$

These equations are derived by taking the arc length derivative (denoted by $\dot{}$) of force and moment balances on an arbitrary section of rod as shown in Fig. 1. The internal force and moment vectors in the rod at arc length s are denoted by the vectors $\boldsymbol{n}$ and $\boldsymbol{m}$. The position is $\boldsymbol{r}$, $\boldsymbol{f}$ is an applied force distribution per unit of s, and $\boldsymbol{l}$ is an applied moment distribution. These general equations can be adapted to describe the full spatial deformations of many different continuum robot architectures.

We will use a simplified model in our simulations by restricting the robot's motion to a plane, neglecting transverse shear strain and axial extension, and considering external loads only at the end effector. Specifically, this results in a model similar to that used in much of Gravagne and Walker's work [12], [13], where the robot structure consists of a planar elastica acted on by actuator torques at discrete points along the length. In the case where there are no external loads, this model reduces to the piecewise constant-curvature result that has been experimentally validated by several groups (see, e.g. [13], [14]) using robots driven by tendon wires, such as the one shown in Fig. 2.

Our simplified robot model is pictured in Fig. 2 with its kinematic variables x, y, the tangent angle θ, actuator torques τ_1, τ_2, and external tip force components F_x and F_y. Assuming a linear constitutive law, the internal bending moment in the backbone at s is proportional to the curvature

$$\boldsymbol{m} = [0 \quad 0 \quad EIu]^T \tag{4}$$

where E is Young's modulus, I is the second moment of area of the backbone cross section about the z axis, and $u(s) \equiv \frac{d\theta}{ds}$ is the curvature of the rod. Assuming

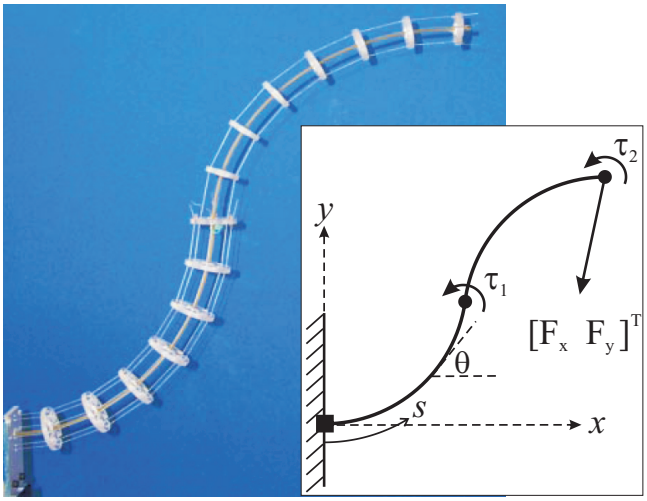

Fig. 2. A tendon driven continuum robot prototype and a schematic of our planar robot model with actuation torques and tip forces (Prototype picture adapted from [13]).

that there are no distributed loads, the internal force vector will be:

$$\boldsymbol{n} = [F_x \quad F_y \quad 0]^T, \tag{5}$$

and the backbone position is differentially related to the tangent angle θ as follows:

$$\begin{aligned} \boldsymbol{r} &= [x \quad y \quad 0]^T, \\ \dot{\boldsymbol{r}} &= [\cos(\theta) \quad \sin(\theta) \quad 0]^T. \end{aligned} \tag{6}$$

Thus, using (3), we arrive at a set of first order differential equations describing the shape of the robot as follows:

$$\begin{aligned} \dot{x} &= \cos(\theta) \\ \dot{y} &= \sin(\theta) \\ \dot{\theta} &= u \\ \dot{u} &= \frac{1}{EI}\left(F_x \sin(\theta) - F_y \cos(\theta)\right). \end{aligned} \tag{7}$$

The boundary conditions for this system are given by:

$$\begin{aligned} x(0) &= 0 \\ y(0) &= 0 \\ \theta(0) &= 0 \\ u^+(L/2) &= u^-(L/2) - \frac{\tau_1}{EI} \\ u(L) &= \frac{\tau_2}{EI}, \end{aligned} \tag{8}$$

where $-$ and $+$ superscripts indicate the value as approached from the left and the right. This boundary value problem can be solved using a variety of numerical methods. In the simulations that follow, we use a shooting method, which consists of iteratively guessing

a value for $u(0)$, solving the resulting initial value problem with a Runge-Kutta method, and checking to see if the boundary condition for $u(L)$ is satisfied. A nonlinear root-finding algorithm can be used to quickly converge on the correct guess for $u(0)$.

The above procedure for calculating the robot's end effector pose $\boldsymbol{p} = [x \quad y \quad \theta]^T$ as a function of the actuator values $\boldsymbol{\tau} = [\tau_1 \quad \tau_2]^T$ and applied loads $\boldsymbol{F} = [F_x \quad F_y]^T$ will hereafter be referred to as the forward kinematic mapping $\boldsymbol{p} = \boldsymbol{g}(\boldsymbol{\tau}, \boldsymbol{F})$.

A. The Jacobian and Compliance Matrices

In our Extended Kalman Filter, we will employ two matrices which can be computed using the model above. First, the robot's Jacobian matrix relates how the pose variables change with respect to changes in the actuation variables τ_1, and τ_2, as

$$J = \begin{bmatrix} \frac{\partial x}{\partial \tau_1} & \frac{\partial x}{\partial \tau_2} \\ \frac{\partial y}{\partial \tau_1} & \frac{\partial y}{\partial \tau_2} \\ \frac{\partial \theta}{\partial \tau_1} & \frac{\partial \theta}{\partial \tau_2} \end{bmatrix}. \tag{9}$$

Similarly, the robot's compliance matrix relates pose changes to changes in the external loads F_x, and F_y, as

$$C = \begin{bmatrix} \frac{\partial x}{\partial F_x} & \frac{\partial x}{\partial F_y} \\ \frac{\partial y}{\partial F_x} & \frac{\partial y}{\partial F_y} \\ \frac{\partial \theta}{\partial F_x} & \frac{\partial \theta}{\partial F_y} \end{bmatrix}. \tag{10}$$

Both J and C are functions of $\boldsymbol{\tau}$ and $\boldsymbol{F}$, and they may be computed approximately via finite differences using the forward kinematic model, or via integration of additional equations as described in [15].

We will use these matrices in the prediction step of our Extended Kalman Filter algorithm, which maps uncertainty in the actuator and force values to a resulting uncertainty in the pose, as discussed in the next section.

B. Robot Parameters and Uncertainty

In this section, we will define some specific robot parameters in order to investigate and visualize the effects of actuation and applied force uncertainty on a specific continuum robot. For the prototype robot investigated in [10], its central backbone is a spring steel rod (ASTM A228) of length $L = 242$ mm and diameter $d = 0.8$ mm with a Young's modulus of $E = 210$ GPa. This results in a bending stiffness of $EI = 0.0042\ Nm^2$.

Suppose that $\boldsymbol{F} = [0 \quad 0]^T$ is known, and the uncertainty in $\boldsymbol{\tau} = [\tau_1 \quad \tau_2]^T$ is Gaussian with mean

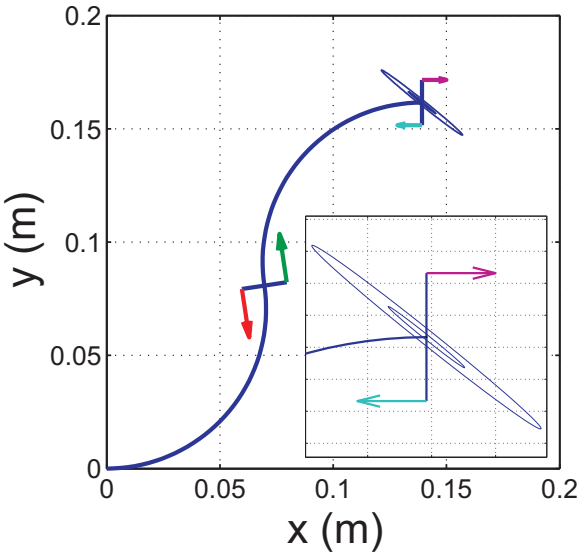

Fig. 3. The σ and 3σ Gaussian uncertainty ellipses for the tip position are plotted assuming the symmetric Gaussian distribution for τ_x and τ_y given in (11).

and covariance,

$$\begin{aligned} \boldsymbol{\mu}_\tau &= [120 \quad -60]^T \quad mNm \\ \Sigma_\tau &= \begin{bmatrix} 1 & 0 \\ 0 & 1 \end{bmatrix} \quad (mNm)^2. \end{aligned} \tag{11}$$

Then, using a linearized approximation of the forward kinematic mapping (which is assumed to be a good approximation over the region of uncertainty) the resulting probability distribution for $\boldsymbol{p}$ will be Gaussian with mean and covariance given by the model prediction step of the conventional EKF, using the forward kinematic mapping and the Jacobian matrix,

$$\begin{aligned} \boldsymbol{\mu_p} &= \boldsymbol{g}(\boldsymbol{\mu}_\tau, \mathbf{0}) \\ \Sigma_p &= J \Sigma_\tau J^T. \end{aligned} \tag{12}$$

The eigenvectors of Σ_p provide the directions of the principal axes of an uncertainty ellipsoid for $\boldsymbol{p}$, and the square roots of the corresponding eigenvalues give the axis lengths for one standard deviation, σ, away from the mean. Plotting the resulting σ and 3σ uncertainty ellipses for the robot's tip position in Fig. 3, we see that the resulting tip uncertainty is much larger in one direction, illustrating that the Jacobian is ill-conditioned.

Similarly, if $\boldsymbol{\tau}$ is known, and the uncertainty in the applied force is described by a Gaussian distribution with mean and covariance,

$$\begin{aligned} \boldsymbol{\mu}_F &= [0 \quad 0]^T \quad mN \\ \Sigma_F &= \begin{bmatrix} 100 & 0 \\ 0 & 100 \end{bmatrix} \quad mN^2, \end{aligned} \tag{13}$$

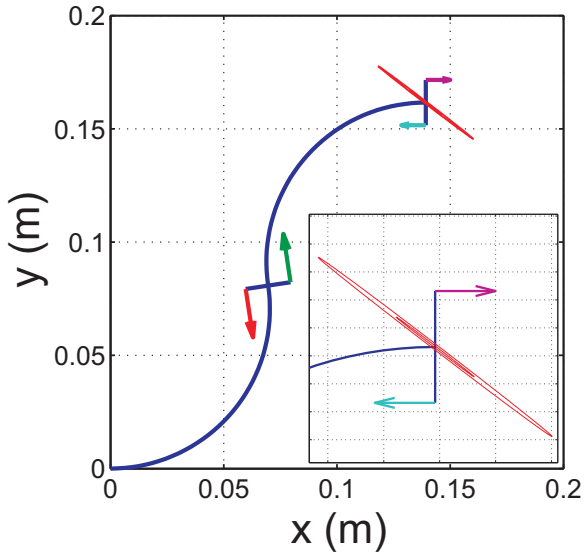

Fig. 4. The σ and 3σ Gaussian uncertainty ellipses for the tip position are plotted assuming the symmetric Gaussian distribution for F_x and F_y given in (13).

then the resulting mean and covariance for $\boldsymbol{x}$ are

$$\begin{aligned} \boldsymbol{\mu_p} =& \boldsymbol{g}(\boldsymbol{\tau}, \boldsymbol{\mu}_F) \\ \Sigma_p =& C\Sigma_F C^T, \end{aligned} \tag{14}$$

and the resulting position ellipses are plotted in Fig. 4. The ill-conditioned nature of J and C exhibited in both plots makes deflection-based force sensing a challenging task because a small amount of inaccuracy in the pose measurement may lead to either a large or small error in the force estimation. This fact highlights the need to approach deflection-based force sensing from a probabilistic perspective, and the importance of quantifying the uncertainty of force estimates that are based on measurements of the tip pose.

III. Extended Kalman Filter Approach

The conventional Extended Kalman Filter algorithm is based on a Hidden Markov Model for the robot's motion, where the current robot state $\boldsymbol{x}_t$ is a function of the previous state $\boldsymbol{x}_{t-1}$ and the current control input $\boldsymbol{u}_t$. Sensors provide measurements of quantities that are functions of the robot's state $\boldsymbol{z}_t = \boldsymbol{h}(\boldsymbol{x}_t)$. The EKF algorithm determines a Gaussian probability distribution for the current state given the previous state's distribution, the current control input, and the current sensor data, i.e.,

$$(\boldsymbol{\mu}_t, \boldsymbol{\Sigma}_t) = \text{EKF}\left(\boldsymbol{\mu}_{t-1}, \boldsymbol{\Sigma}_{t-1}, \boldsymbol{u}_t, \boldsymbol{z}_t\right). \tag{15}$$

For a continuum robot model of the form in (1), the probability distributions for $\boldsymbol{p}$, $\boldsymbol{\tau}$, and $\boldsymbol{F}$ must be dependent because these quantities are all related through the forward kinematic model. This leads us to define our state vector as

$$\boldsymbol{x} = [\boldsymbol{p} \quad \boldsymbol{\tau} \quad \boldsymbol{F}]^T, \tag{16}$$

which allows us to estimate the combination of $\boldsymbol{p}$, $\boldsymbol{\tau}$, and $\boldsymbol{F}$ simultaneously. In this formulation, the control input has been subsumed into the state vector.

Our sensor measurements consist of the tip pose and actuator values, so that $\boldsymbol{z}_t = H\boldsymbol{x}_t$, where

$$H = \begin{bmatrix} I_{5\times5} & 0_{5\times2} \end{bmatrix}, \tag{17}$$

and we assume that the uncertainty in these measurements is Gaussian with a covariance matrix Q, using the values below as a base-line for our simulations in the following section,

$$Q = \begin{bmatrix} 1\ mm^2 & 0 & 0 & 0 & 0 \\ 0 & 1\ mm^2 & 0 & 0 & 0 \\ 0 & 0 & 1\ deg^2 & 0 & 0 \\ 0 & 0 & 0 & 1\ (mNm)^2 & 0 \\ 0 & 0 & 0 & 0 & 1\ (mNm)^2 \end{bmatrix}. \tag{18}$$

In this formulation, we assume any modeling inaccuracy is represented in the measurement uncertainty. Future work may address how to explicitly incorporate uncertainty arising from model parameters or the structure of the model itself into the EKF framework.

The EKF requires an input mean $\boldsymbol{\mu}_i = \begin{bmatrix} \boldsymbol{\mu}_{ip}^T & \boldsymbol{\mu}_{i\tau}^T & \boldsymbol{\mu}_{iF}^T \end{bmatrix}^T$ and input covariance matrix $\boldsymbol{\Sigma}_i$. In our simulations we use the current sensor measurements $\boldsymbol{z}_t$ for $\boldsymbol{\mu}_{ip}$ and $\boldsymbol{\mu}_{i\tau}$, the previous estimate of the force for $\boldsymbol{\mu}_{iF}$, and the following input covariance matrix

$$\Sigma_{input} = \begin{bmatrix} Q & 0 & 0 \\ 0 & 100\ mN^2 & 0 \\ 0 & 0 & 100\ mN^2 \end{bmatrix}. \tag{19}$$

We now state the EKF algorithm explicitly:

$$\begin{aligned} (\boldsymbol{\mu}_t, \boldsymbol{\Sigma}_t) &= \text{EKF}(\boldsymbol{\mu}_i, \boldsymbol{\Sigma}_i, \boldsymbol{z}_t) \\ \overline{\boldsymbol{\mu}} &= \begin{bmatrix} \boldsymbol{g}(\boldsymbol{\mu}_{\tau i}, \boldsymbol{\mu}_{Fi})^T & \boldsymbol{\mu}_{\tau i}^T & \boldsymbol{\mu}_{Fi}^T \end{bmatrix}^T \\ G &= \begin{bmatrix} 0_{3\times3} & J & C \\ 0_{4\times3} & & I_{4\times4} \end{bmatrix} \\ \overline{\Sigma} &= G\Sigma_i G^T \\ K &= \overline{\Sigma} H^T (H\overline{\Sigma}H^T + Q)^{-1} \\ \boldsymbol{\mu}_t &= \overline{\boldsymbol{\mu}} + K(\boldsymbol{z}_t - \boldsymbol{h}(\overline{\boldsymbol{\mu}})) \\ \Sigma_t &= (I - KH)\overline{\Sigma}. \end{aligned} \tag{20}$$

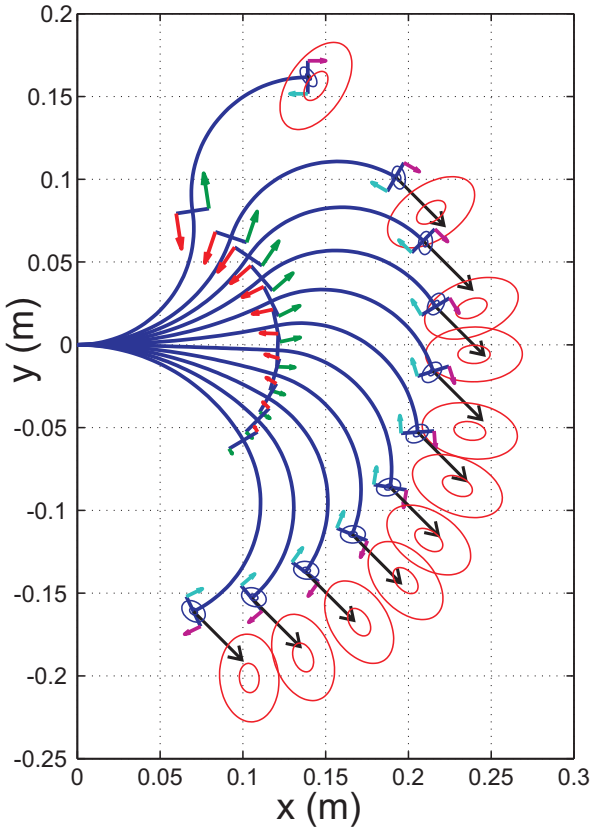

Fig. 5. In this simulation, the applied tip force suddenly changes from zero to $[30\ -30]^T\ mN$, while the actuators are continually moving the robot from the top to the bottom of the figure. The EKF force estimates are represented by the red σ and 3σ ellipses near the tip of the force vectors.

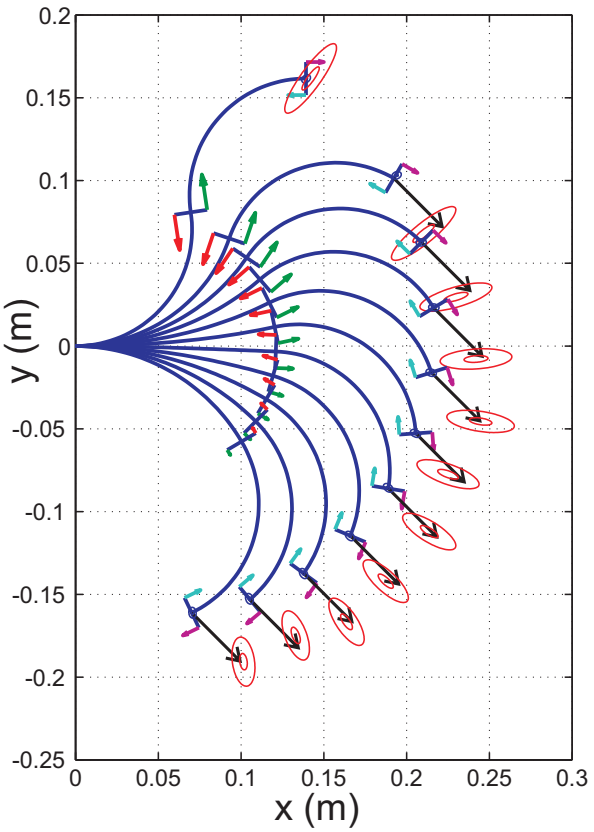

Fig. 6. The same scenario as Fig. 7 is shown, but with higher sensor accuracy (simulated by averaging the last ten sensor measurements) and with Q/10 used in the algorithm.

IV. Simulation Results

We tested the algorithm given in Section III with simulated noisy measurements of the tip coordinates and actuator values sampled from Gaussian distributions. Two test cases were performed. The first simulates a sudden change in the applied force from zero to $[30\ -30]^T\ mN$. After this, the forces remain constant but the robot's actuators continually move the robot. This case is illustrated in Fig. 5 and Fig. 6. The robot's ground truth shape is plotted, along with a black vector at the tip which represents the applied force. The blue ellipses around the tip of the robot are the σ and 3σ uncertainty ellipses for the tip position, and the red ellipses near the tip of the applied force vector are the σ and 3σ uncertainty ellipses for the location of the tip of the force vector, output from the EKF.

Fig. 5 shows the result when the sensor accuracy is that of (18). In Fig. 6, a more accurate sensor was simulated by averaging the previous ten measurements at each time step, and the Q from (18) was accordingly replaced with $Q/10$ (since the variance of the sample mean of a Gaussian scales inversely with the number of samples). The result in Fig. 6 is higher accuracy, but the accuracy is more dependent on the direction, as shown by the smaller, yet flatter ellipses.

The second test case is shown in Fig. 7, and 8. The actuators remain at fixed values, and the force was increased from 0 to $[100\ -100]^T\ mN$ in increments of $[20\ -20]^T\ mN$ at each time step. This represents a difficult scenario for force estimation, since the force is applied in a direction in which the robot is much stiffer (corresponding to the short axis of the ellipse in Fig. 4). In this case, Fig. 7 shows that the measurement accuracy (Q in (18)) is insufficient for quick convergence of the EKF algorithm. In Fig. 8, convergence is achieved by increasing the sensor accuracy (by averaging the previous 100 measurements), and using $Q/100$ in the EKF, indicating that high measurement accuracy may be needed for good performance in some cases.

V. Conclusions

The results in Section IV show that using an Extended Kalman Filter approach is feasible for

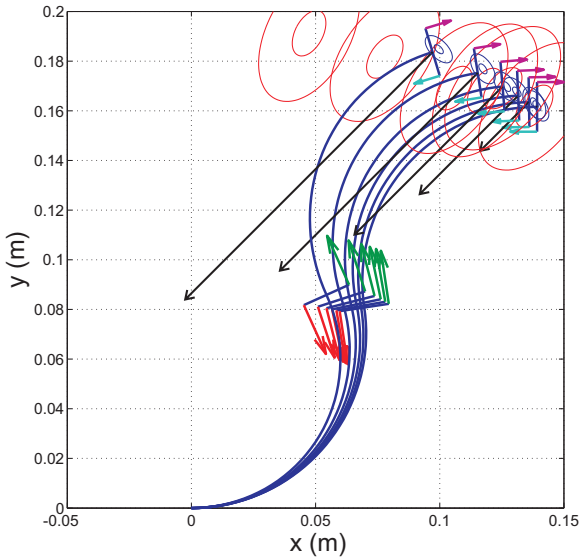

Fig. 7. The applied tip force continually increases in a direction in which the robot is relatively stiff. This leads to poor convergence when the sensor accuracy is not high enough.

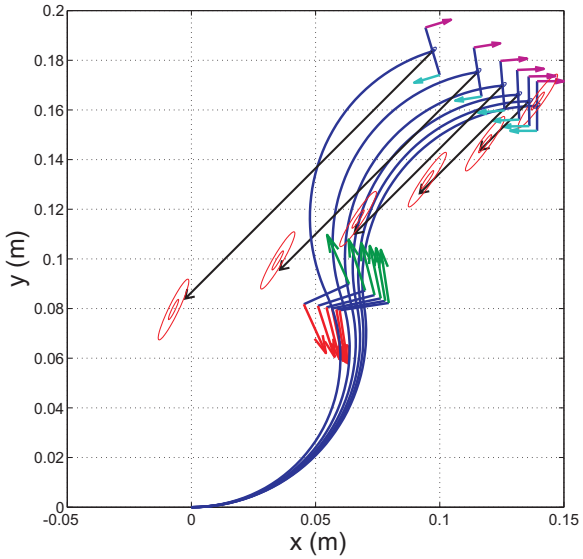

Fig. 8. The same scenario as Fig. 7 is shown, except with a higher sensor accuracy (simulated by averaging the previous 100 measurements), and with Q/100 used in the algorithm.

deflection-based force sensing using continuum robots, which, as we showed in Section II, often have ill-conditioned compliance matrices and Jacobians. There is much future work to be done, including developing guidelines for how accurate sensors must be for various kinds of robots in various configurations to achieve force sensing, and when it may not be possible in certain directions (this is analogous to the sensable and insensable wrenches seen in prior continuum robot work [5]). Also, experimental validation of sensed forces against known applied forces is essential, and experiments will be conducted in the near future. We also intend to extend this work to consider many loads along the robot (not just at the tip), test the method on other continuum robot types, and apply it to non-planar robot configurations. The work in this paper serves as a first step toward these future goals.

REFERENCES

[1] R. J. Webster III and B. A. Jones, "Design and kinematic modeling of constant curvature continuum robots: A review," *International Journal of Robotics Research*, vol. 29, pp. 1661–1683, 2010.

[2] D. Trivedi, C. D. Rahn, W. M. Kierb, and I. D. Walker, "Soft robotics: Biological inspiration, state of the art, and future research," *Applied Bionics and Biomechanics*, vol. 5, no. 3, pp. 99 – 117, 2008.

[3] G. Robinson and J. B. C. Davies, "Continuum robots – a state of the art," *IEEE International Conference on Robotics and Automation*, pp. 2849–2854, 1999.

[4] K. Xu and N. Simaan, "An investigation of the intrinsic force sensing capabilities of continuum robots," *IEEE Transactions on Robotics*, vol. 24, no. 3, pp. 576–587, 2008.

[5] ——, "Intrinsic wrench estimation and its performance index for multisegment continuum robots," *IEEE Transactions on Robotics*, vol. 26, no. 3, pp. 555–561, 2010.

[6] A. Bajo and N. Simaan, "Finding lost wrenches: Using continuum robots for contact detection and estimation of contact location," *IEEE International Conference on Robotics and Automation*, pp. 3666–3673, 2010.

[7] D. C. Rucker, B. A. Jones, and R. J. Webster III, "A geometrically exact model for externally loaded concentric-tube continuum robots," *IEEE Transactions on Robotics*, vol. 26, pp. 769–780, 2010.

[8] D. Trivedi, A. Lotfi, and C. D. Rahn, "Geometrically exact models for soft robotic manipulators," *IEEE Transactions on Robotics*, vol. 24, pp. 773 – 780, 2008.

[9] B. Jones, R. Gray, and K. Turlapati, "Three dimensional statics for continuum robotics," *IEEE/RSJ International Conference on Intelligent Robots and Systems*, pp. 2659–2664, 2009.

[10] D. C. Rucker and R. J. Webster III, "Statics and dynamics of continuum robots with general tendon routing and external loading," *IEEE Transactions on Robotics*, 2011, (In Press).

[11] S. S. Antman, *Nonlinear Problems of Elasticity*, 2nd ed., S. Antman, J. Marsden, and L. Sirovich, Eds. Springer Science, 2005.

[12] I. A. Gravagne and I. D. Walker, "Manipulability, force, and compliance analysis for planar continuum robots," *IEEE Transactions on Robotics and Automation*, vol. 18, no. 3, pp. 263–273, 2002.

[13] I. A. Gravagne, "Design, analysis and experimentation: the fundamentals of continuum robotic manipulators," Ph.D. dissertation, Clemson University, 2002.

[14] D. B. Camarillo, C. F. Milne, C. R. Carlson, M. R. Zinn, and J. K. Salisbury, "Mechanics modeling of tendon-driven continuum manipulators," *IEEE Transactions on Robotics*, vol. 24, no. 6, pp. 1262–1273, 2008.

[15] D. C. Rucker and R. J. Webster III, "Computing Jacobians and compliance matrices for externally loaded continuum robots," *IEEE International Conference on Robotics and Automation*, 2011.